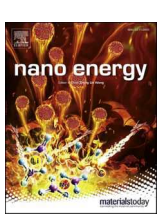
ELSEVIER

Contents lists available at ScienceDirect

Nano Energy

journal homepage: http://www.elsevier.com/locate/nanoen





Ultra-thin dark amorphous ${\rm TiO}_x$ hollow nanotubes for full spectrum solar energy harvesting and conversion ‡

Youhai Liu^{a,1}, Haomin Song^{a,1}, Zongmin Bei^b, Lyu Zhou^a, Chao Zhao^{c,2}, Boon S. Ooi^c, Qiaoqiang Gan^{a,*}

- ^a Department of Electrical Engineering, The State University of New York at Buffalo, Buffalo, NY 14260, USA
- b Shared Instrumentation Laboratories, School of Engineering & Applied Sciences, The State University of New York at Buffalo, Buffalo, NY 14260, USA
- c KAUST Photonics Lab, King Abdullah University of Science and Technology, Thuwal 23955-6900, Saudi Arabia

ARTICLE INFO

Keywords: Dark TiO_x Atomic layer deposition Ultra-thin films Photocatalysis Photothermal effects

ABSTRACT

Dark titania (TiO_x) have been widely used for solar energy harvesting and conversion applications due to its excellent light absorbing performance throughout the ultraviolet to near infrared wavelength band, low cost, and non-toxic nature. However, the synthesis methods of dark TiO_x are usually complicated and time-consuming. Here we report a facile and rapid method to fabricate dark amorphous TiO_x (am- TiO_x) hollow nanotube arrays on nanoporous anodic alumina oxide (AAO) templates using atomic layer deposition. Systematic investigation was performed to demonstrate that Ti^{3+} and O species in the am- TiO_x ultra-thin films, as well as the spatial distribution of these am- TiO_x ultra-thin films on the vertical side walls of AAO templates are two major mechanisms of the black color. Importantly, the film deposition took ~18 min only to produce the optimized ~4- nm-thick am- TiO_x film. Representative applications were demonstrated using photocatalytic reduction of silver nitrate and photothermal solar vapor generation, revealing the potential of these ultra-thin dark am- TiO_x /AAO structures for full spectrum solar energy harvesting and conversion.

1. Introduction

 TiO_2 is one of the most important semiconductor materials for energy harvesting and conversion due to its earth abundance, low cost and non-toxic nature [1]. However, the well-known photocatalyst TiO_2 absorbs ultraviolet (UV) light only (i.e., less than 5% of the solar energy) [2], thus limiting its overall conversion efficiency for solar energy. Since the seminal report on UV photoelectrochemical water splitting using TiO_2 as photoanodes [3], much effort has been devoted to enhance its optical absorption in visible and near infrared (IR) domain (i.e., to realize dark TiO_2 materials [1,2,4]) for full spectrum solar energy harvesting and conversion applications [5–7]. However, the synthesis methods of dark TiO_2 are usually complicated and time-consuming. For instance, in the first report to obtain the so-called black TiO_2 , TiO_2 nanocrystals were hydrogenated at 200 °C for 5 days [8]. TiO_x nanoparticles (NPs) were synthesized using magnesium reduction under Ar atmosphere at 600 °C for 4 h [9]. Dark TiO_2 NPs were realized via

chemical reduction followed by calcination under Ar atmosphere for 4 h [10]. Physical means were also employed to obtain nanosized titanium sesquioxide (Ti_2O_3) powders for solar thermal applications [11].

To enable the development of applications using dark ${\rm TiO_x}$ materials, it is important to recognize the intrinsic trade-off between their optical absorption and electronic properties: i.e., an optical absorber should be thick enough to absorb the majority of the incident light but thin enough to allow the carrier extraction. Therefore, the ultimate goal is to realize super-efficient solar absorption within ultra-thin ${\rm TiO_x}$ films. In the past decade, various photonic strategies have been proposed to enhance the light-matter interaction within thin film semiconductor materials down to atomic layer thicknesses (e.g [12,13].). For instance, engineered photonic crystal cavities [14,15] and plasmonic nanopatterns [16,17] were widely used to enhance the optical absorption within ultra-thin semiconductors (including two-dimensional materials). In particular, two- to three-layered planar nanocavity architectures were successfully implemented to enhance the optical absorption within ultra-thin Ge

^{*} Corresponding author.

E-mail address: qqgan@buffalo.edu (Q. Gan).

¹ These authors contribute equally to this work.

² Current address: Key Laboratory of Semiconductor Materials Science, Institute of Semiconductors, Chinese Academy of Sciences & Beijing Key Lab of Low Dimensional Semiconductor Materials and Devices, Beijing 100083, China.

films [18–20], Fe $_2$ O $_3$ films [21], FePt films [22], 2D materials [23,24], as well as TiO $_2$ films [25]. By controlling the optical interference condition within the nanocavity structure, over 90% of UV light was absorbed by a 2-nm-thick TiO $_2$ films, and, therefore, resulting in a 1000 \times more efficient photocatalytic reaction for CO $_2$ reduction than conventional PM25 TiO $_2$ particles [25]. The next intriguing question is whether a full spectral solar harvesting and conversion can be realized using these ultra-thin semiconductor films.

Here we report a facile and rapid method to realize dark amorphous ${\rm TiO}_{\rm X}$ (am- ${\rm TiO}_{\rm X}$) hollow nanotube architecture by directly depositing ultrathin ${\rm TiO}_{\rm X}$ films (i.e., 2 nm \sim 10 nm) on porous anodic aluminum oxide (AAO) templates using atomic layer deposition (ALD) processes. Due to the three-dimensional structural feature and existence of ${\rm Ti}^{3+}$ and O species, the am- ${\rm TiO}_{\rm X}$ nanotube array with the optimized thickness of \sim 4 nm shows broadband strong optical absorption throughout the entire solar spectrum. Remarkably, this ultra-thin film ALD process took \sim 18 min only. This type of inexpensive three-dimensional am- ${\rm TiO}_{\rm X}$ hollow nanotube array over large areas enables the development of practical full spectrum solar-thermal and photocatalytic applications, as will be validated by the visible-to-IR photocatalytic reduction of silver nitrate and photothermal solar vapor generation.

2. Results and discussion

ALD is outstanding in producing uniform and conformal thin films. It has been used for coatings on various structures including nanostructured surfaces (e.g [26–28]., particularly on nanorods [29] and AAO substrates; [30,31] see details in Section S1 in the Supporting Information). A typical process to fabricate TiO_2 films in an ALD system employs two precursors, one providing the Ti element and the other offering the O element [i.e., tetrakis(dimethylamido)-titanium (Ti(N (CH)₃)₂)₄ (TDMAT), and water (H₂O) in this work, see details in the Experimental Section]. A single ALD cycle typically consists of a sequential injection and purge of TDMAT and H₂O. After the reaction of a single ALD cycle, the following process will occur: [32].

$$Ti(N(CH)_3)_2)_4 + 2H_2O \rightarrow TiO_2(solid) + 4NH(CH_3)_2$$
 (1)

Under a suitable reaction condition (e.g. the system was maintained at 90 °C with a 0.2-s water pulse followed by a 7-s reaction and a 0.4-s TDMAT pulse followed by a 10-s reaction [28]), a monolayer of TiO₂ will form on the substrate while other reactants and products will be purged away. By controlling the ALD cycles, the thickness of the planar TiO2 film can be controlled accurately down to Angstrom level (e.g. [33].). We employed this process to produce planar 2-nm-thick TiO₂ films for efficient photocatalytic applications driven by UV light [25]. However, when defect species are introduced in TiO₂ (e.g. Ti³⁺ or O⁻), new defect states will generate in the bandgap of TiO2, resulting in different optical properties of the deposited films (corresponding to the color change). In particular, by controlling the density of defect states, the color of TiO_x can even be tuned to black (e.g [34,35].). It was reported that these defect species are highly related to the reaction temperature and pressure, reaction atmosphere, precursor selection, etc. Sophisticated process controls were usually required to produce dark TiO_x materials (e.g. hydrogenation [8], chemical reduction [9], chemical oxidation [36], electrochemical reduction [37], ionothermal process [38], laser ablation [39], microwave radiation [40], and ultrasonication [41]). Here we will report a facile method to realize dark TiO_x nanotube arrays on nanoporous substrates using a one-step ALD process.

2.1. Dark am- TiO_x hollow nanotube arrays: a one-step ALD process

Recently, dark TiO_2 nanotubes were reported using anodic TiO_2 nanotube layers treated by advanced processes using sophisticated facilities (e.g. high pressure H_2 treatment [42], high energy proton implantation [43], melted aluminum reduction [44], femtosecond laser

mediated fabrication [45], etc.). Simpler and more rapid manufacturing methods are highly desired. In our experiment, three substrates were placed in the chamber to deposit TiOx films through the same ALD process, i.e., a silicon wafer, a glass substrate and a nanoporous AAO template. Fig. 1A illustrates the ALD process on nanopores (each cycle takes ~10 s in our optimal ALD process, see fabrication details in the Experimental Section). After the deposition of a 10-nm-thick TiO_x film (i.e., 260 cycles with the entire deposition time of ~44 min), the TiOx/AAO sample became visibly black, surprisingly different from the planar TiOx/glass sample fabricated in the same batch (as shown in Fig. 1B). The microscopic top- and side-view of the AAO substrate taken by scanning electron microscopy (SEM, see details in the Experimental Section) are shown in Fig. 1C and 1E, respectively. The average pore diameter and the pore-to-pore distance of the AAO template are ~400 nm and ~450 nm, respectively. The vertical dimension of the AAO template is $\sim 50 \, \mu m$. Since this type of AAO structure is highly scattering, we employed an integration sphere spectroscope to measure its optical absorption accurately (see details in the Experimental Section). As shown in Fig. 1D, the absorption of a bare AAO template is less than 0.1 in the visible to near IR range (blue curve). Surprisingly, the averaged optical absorption of the coated AAO template is ~0.95 (red curve) throughout the entire visible to near IR range, which renders the sample visibly different from previously reported dense and aligned TiO2 nanotube arrays [30]. This strong absorption enhancement should be attributed to the TiOx thin films coated on the AAO top and vertical surfaces, as illustrated by the inset of Fig. 1D. To reveal the film penetration into the vertical pores, we employed the energy dispersive X-ray spectroscopy (EDS) to analyze the element distribution (see details in the Experimental Section). As shown in Fig. 1F, the distribution of titanium element demonstrates the full coverage of TiO_x on the side walls. Besides, the oxygen (Fig. 1G) and the aluminum element (Fig. 1H) were from the AAO templates. This TiO_x hollow nanotube architecture should be responsible for the dark color of the TiOx/AAO template due to their unique chemical and structural properties.

2.2. Chemical properties

To reveal the mechanism of this dark TiOx/AAO template, we first characterized the dispersive optical constants (i.e., refractive index, n, and absorption coefficient, k) of a 10 nm-thick TiO_x film deposited on a silicon wafer fabricated in the same ALD process (solid curves in Fig. 2A). As shown by the solid blue curve, this film shows stronger absorption than that of regular TiO2 films (the dashed blue curve adapted from [46]), indicating that the chemical feature of this ALD-deposited TiO_x film is significantly different from crystalized TiO₂. To confirm this prediction, we employed a Raman spectroscopic microscope to characterize this sample. As shown in Fig. 2B, no obvious peak was observed in the Raman spectrum of the dark TiO_x/AAO template (black curve), indicating the amorphous phase of TiO_x (similar to results reported in [47]). We also performed thermal annealing of the dark TiO_x/AAO template at 300 °C for 1 h and 600 °C for 20 h, respectively. One can see from the insets in Fig. 2B that the color was tuned to yellow and white, respectively (see their absorption spectra in Section S2 in the Supporting Information). Obvious Raman peak at $147~\text{cm}^{\text{-}1}$ appeared on the yellow sample annealed at 300 $^{\circ}\text{C}$ (yellow curve). Other peaks at 398 cm⁻¹, 516 cm⁻¹, and 640 cm⁻¹ (grey curve) were observed on the white sample annealed at 600 °C, indicating the anatase phase of typical crystalized TiO2 films [47]. We further investigated the Raman peak in the range of 100 cm⁻¹ to 185 cm⁻¹ in Fig. 2C (i.e., the peak in the red rectangle in Fig. 2B). A red shift of the Raman peak was observed from 147 cm⁻¹ to 144 cm⁻¹, agreeing with the observation reported in ref [48]. In addition, the results of X-ray diffraction (XRD) analysis agreed well with that of the Raman spectra, confirming the phase change due to annealing (see details in Section S3 in the Supporting Information).

To further confirm the amorphous phase of the dark TiOx/AAO

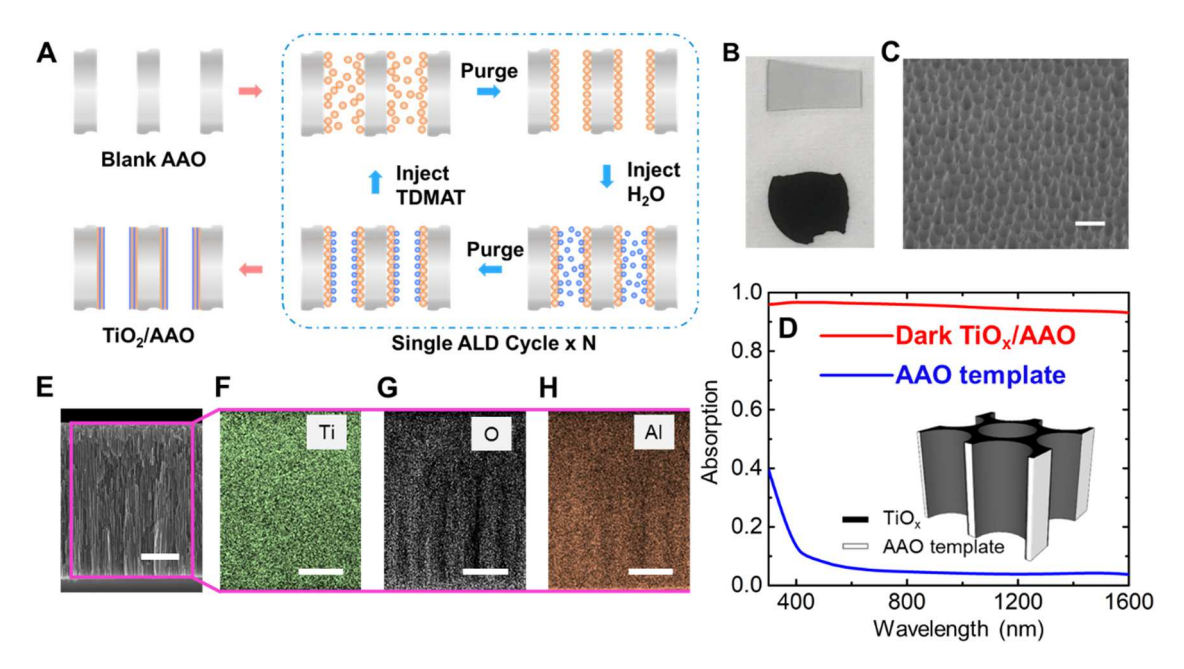


Fig. 1. (a) Schematic of the ALD process. (b) The photograph of the TiO_x /glass (top) and the dark TiO_x /AAO (bottom). (c) The top-view SEM image of the AAO template. Scale bar: 1 μ m. (d) Measured optical absorption spectra of the bare AAO template (blue) and the dark TiO_x /AAO (red). Inset: Schematic structure of the dark TiO_x /AAO. (e) The side-view SEM image of the dark TiO_x /AAO. Scale bar: 10 μ m. (f-h) The side-view EDS element mapping images of the dark TiO_x /AAO for (f) titanium, (g) oxygen, and (h) aluminum, respectively. Scale bar: 10 μ m.

template, TEM characterization was performed as shown in Fig. 2D: no crystalline structure was observed. Then the X-ray photoelectron spectroscopy (XPS) was employed to characterize the chemical composition of the as-deposited dark TiO_x/AAO (i.e., black curves in Fig. 2E and 2F). More characterization details are listed in the Experimental Section. By deconvoluting the obtained XPS spectra, one could analyze the different states of the two main elements, i.e., Ti and O. On one hand, in Fig. 2E, the deconvolution of Ti 2p spectrum from 468 to 452 eV (black curve) led to four peaks at binding energies of 464.1 eV, 462.6 eV, 458.4 eV, and 456.9 eV, corresponding to four coexistent states: Ti⁴⁺ 2p_{1/2} (red curve), Ti³⁺ 2p_{1/2} (magenta curve), Ti⁴⁺ 2p_{3/2} (orange curve), and Ti³⁺ 2p_{3/2} (green curve), respectively [49]. The two Ti⁴⁺ states are typical states associated with Ti⁴⁺-O bonds in TiO₂, which will not result in the black color of the sample. The reduction of Ti⁴⁺ states to the non-stoichiometric Ti3+ states with lower binding energies should account for the absorption enhancement in visible and IR regime. On the other hand, in Fig. 2F, the O 1s spectrum from 536 to 526 eV (black curve) was deconvoluted into two peaks at binding energies of 529.9 eV and 531.2 eV, correlating with O²⁻ (magenta curve) and O⁻ (red curve) states [50], respectively. These two peaks are typically assigned to Ti⁴⁺-O and Ti³⁺-O bonds, respectively. Thus, the higher absorption in visible and IR regime should also be attributed to O states. The existence of O was confirmed by electron paramagnetic resonance (EPR) spectroscopy and resistivity measurement at room temperature (see Experimental Section). In the EPR spectrum of the dark TiOx/AAO (black curve in Fig. 2G), the resonance signal at the index value g of 2.004 corresponds to O⁻ [51]. After annealing, no EPR signal at g of 2.004 was detected (see yellow and grey curves), demonstrating the decrease of the O species (see Section S4 in the supporting information for the molar ratio change of TiO_x). The decrease of the O⁻ species would also lead to changes in the resistivity [52]. Hence, the resistivity of the TiO_x thin film on the glass substrate was investigated after annealing in air at 50 °C, 100 °C, 150 °C, and 200 °C for 30 min (Fig. 2H). The resistivity was stable below 100 °C and increased with the annealing temperature, due to the decrease of O states during the annealing process [52]. Therefore, the high absorption in visible to near IR region should be attributed to the ratio change of the coordination numbers of Ti and O, which is introduced by Ti³⁺ and O in dark TiO_x/AAO.

Importantly, the color of the TiO_x/AAO sample is dependent on the Ti³⁺ and O⁻ species, which can be controlled by two ALD parameters: the first is the amount of injected H₂O, and the second is the reaction time. Following the optimal ALD parameters mentioned in the Experimental Section, the dark TiO_x/AAO was obtained. The average absorption was over 95%, in the visible and near IR range (see the red curve in Fig. 2I, the same as the red curve in Fig. 1D). To tune the parameters, firstly, we injected more H₂O by repeating the water feeding process ten times. In other words, in each cycle, we fed TDMAT once and H₂O ten times. As shown by the photograph in the orange rectangle in Fig. 2I, the sample became grey in color. Its optical absorption decreased, especially in the near IR range (orange curve). Secondly, for each water injection process, the stop valve was closed for 2 s (the purge time was also extended by 2 s for a complete purge) so that TDMAT could react with H₂O for a longer time. As a result, the sample became light grey in color (see the photograph in the grey rectangle in Fig. 2I) with a further dropped optical absorption (grey curve). The molar ratios of these three TiO_x samples were also measured, showing decreased Ti³⁺ and O states (see Section S4 in the Supporting Information). In summary, the amount of H₂O and the reaction time are two key parameters to control Ti³⁺ and O species, and thus to change the darkness of the TiOx/AAO in ALD processes. Although carbon was also observed in element analysis of the AAO scaffold which cannot be completely ruled out from the possible mechanisms responsible for the dark TiO_x/AAO, we performed extra experiments to demonstrate that these carbon residuals are negligible (see Section S5 in the Supporting Information for the thermal gravimetric analysis of TiO_x/AAO).

Importantly, the slightly enhanced absorption coefficient over visible-IR spectral range still did not reveal the complete picture of the dark ${\rm TiO}_x/{\rm AAO}$ template. One can see that the ${\rm TiO}_x$ film deposited on planar substrates did not show dark color (see Fig. 1B). Therefore, another major mechanism is the structural feature.

2.3. Structural properties

To model the optical absorption property of the am- TiO_x/AAO template, we substituted the measured optical constants of the am- TiO_x and the reported data for Al_2O_3 [53] into a simplified nanoporous

Y. Liu et al. Nano Energy 84 (2021) 105872

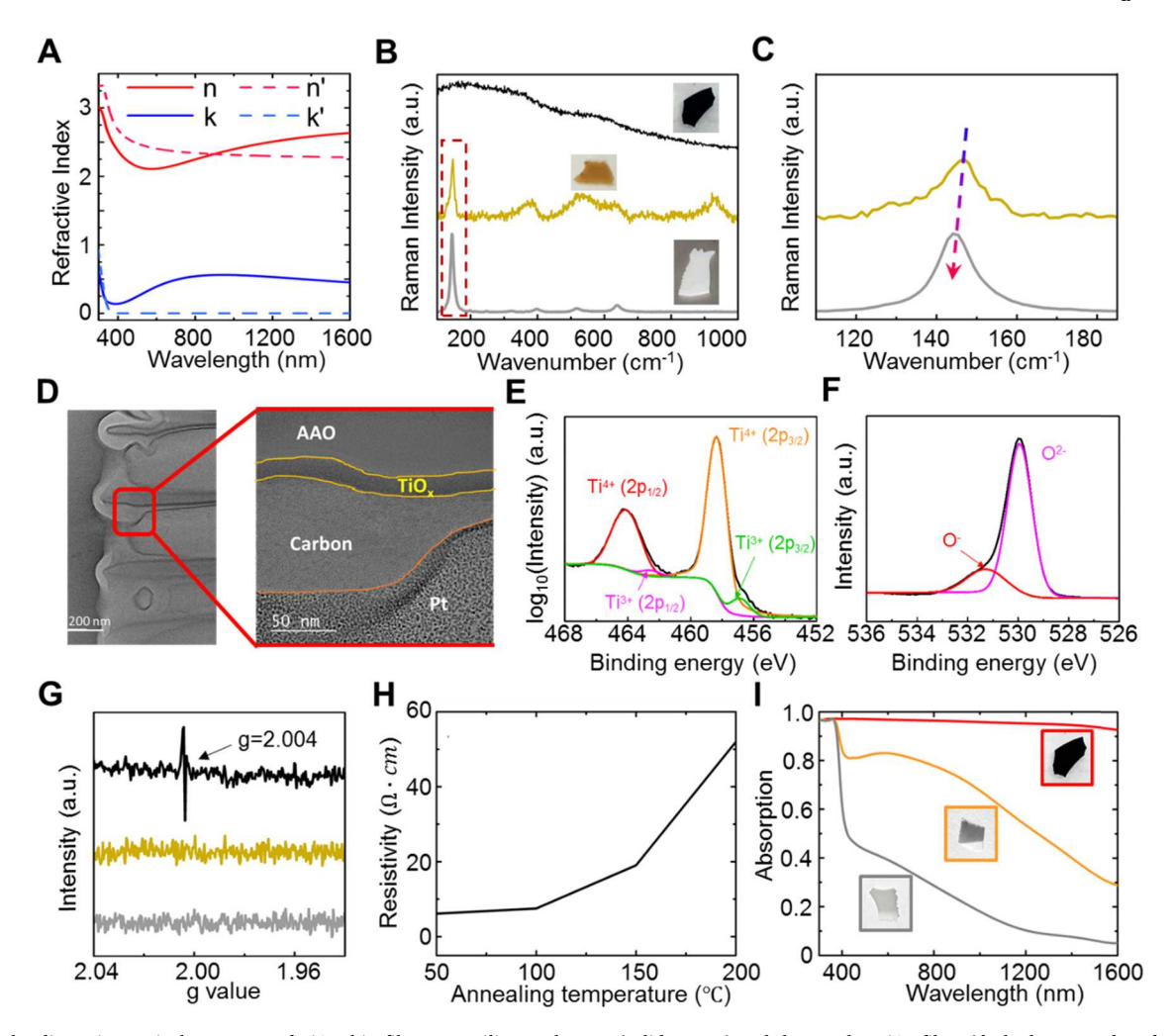


Fig. 2. (a) The dispersive optical constants of TiO_x thin films on a silicon substrate (solid curves) and the regular TiO_2 films (dashed curves, data from [46]). (b) Raman spectra of the dark TiO_x /AAO (black), and the samples after annealing at 300 °C for 1 h (yellow), and 600 °C for 20 h (grey), respectively. Insets: Their corresponding photographs. (c) A zoom-in view of the Raman spectra of the samples after annealing at 300 °C for 1 h (yellow), and 600 °C for 20 h (grey), respectively. The dashed arrow was plotted to guide the eye. (d) Transmission electron microscopy (TEM) images of the dark TiO_x /AAO. The carbon and platinum (Pt) were introduced in the sample preparation process. (e-f) X-ray photoelectron spectroscopy (XPS) spectra and their deconvolution of the dark TiO_x /AAO for (e) Ti 2p and (f) O 1s (g) Electron paramagnetic resonance (EPR) spectra of the dark TiO_x /AAO (black), and the samples after annealing at 300 °C for 1 h (yellow), and 600 °C for 20 h (grey), respectively. (h) The resistivity of the TiO_x on glass substrate after annealing at 50 °C, TiO_x 0 °C, TiO_x 0 °C, TiO_x 0 °C for 30 min (i) Measured optical absorption spectra of samples fabricated under different ALD conditions. Red curve: one-time water injection and 5-s reaction. Orange curve: ten-time water injection and 5-s reaction. Grey curve: ten-time water injection and 9-s reaction. Insets: Corresponding photographs of the three samples to demonstrate the color tunability.

architecture, as illustrated in Fig. 3A. In this architecture, the thickness of am-TiO $_{\rm x}$ was 2 nm. The penetration depth into the vertical direction was tuned from 10 μ m to 30 μ m. To better understand the mechanism for the observed darkness, the absorption in the am-TiO $_{\rm x}$ at the top surface of AAO and along the vertical direction of the nanopores were plotted in Fig. 3B, respectively. Due to the ultra-small thickness (i.e., 2 nm in this modeling), the absorption in the am-TiO $_{\rm x}$ at the top surface (cyan) is small compared with the absorption in the am-TiO $_{\rm x}$ along the vertical direction. The overall optical absorption increases with the larger penetration depth (i.e., the magenta, blue and red curve for 10 μ m, 20 μ m, and 30 μ m, respectively), especially in the visible to near IR region.

To further reveal the spectral response of the optical absorption, we modeled the optical absorption distributions of am-TiO $_{\rm X}$ nanotubes with a penetration depth of 30 µm at the wavelength of 300 nm, 500 nm, 700 nm, 900 nm, and 1100 nm, respectively, in Fig. 3C–G. One can see that as the light propagated downwards, it was absorbed gradually by the ultra-thin film along the vertical direction of the nanopores. Besides, the absorption of light at longer wavelengths (e.g. 500–1100 nm as

shown in Fig. 3D–G) required a greater penetration depth than that for shorter wavelengths (e.g. 300 nm as shown in Fig. 3C). In addition, we also simulated the absorption in the 3-nm- and 4-nm-thick am-TiO $_{\rm x}$ film along the vertical direction of the nanopores with the penetration depth of 30 µm (orange and green curve in Fig. 3B, respectively). These thicker films manifest higher absorption than that in 2-nm-thick am-TiO $_{\rm x}$ films with the same penetration depth (red curve in Fig. 3B). Therefore, greater penetration depths and larger thickness are generally desired to realize broader band optical absorption, as will be validated and optimized experimentally.

Although it is difficult to precisely control the penetration depth of am- ${\rm TiO}_{\rm x}$ films in ALD processes, the gas-phase precursors of the ALD process can penetrate through the nanopores from both top and bottom surfaces of the AAO template and result in a unique controllability. Here we adopted three setups to demonstrate this controllability: Setup A (Fig. 4A) allows the precursors to penetrate into the nanopores from the top surface only; Setup B (Fig. 4B) allows the leakage of precursors from the bottom surface; while Setup C (Fig. 4C) enables free penetration of precursors from the bottom surface of the free-standing AAO template

Y. Liu et al. Nano Energy 84 (2021) 105872

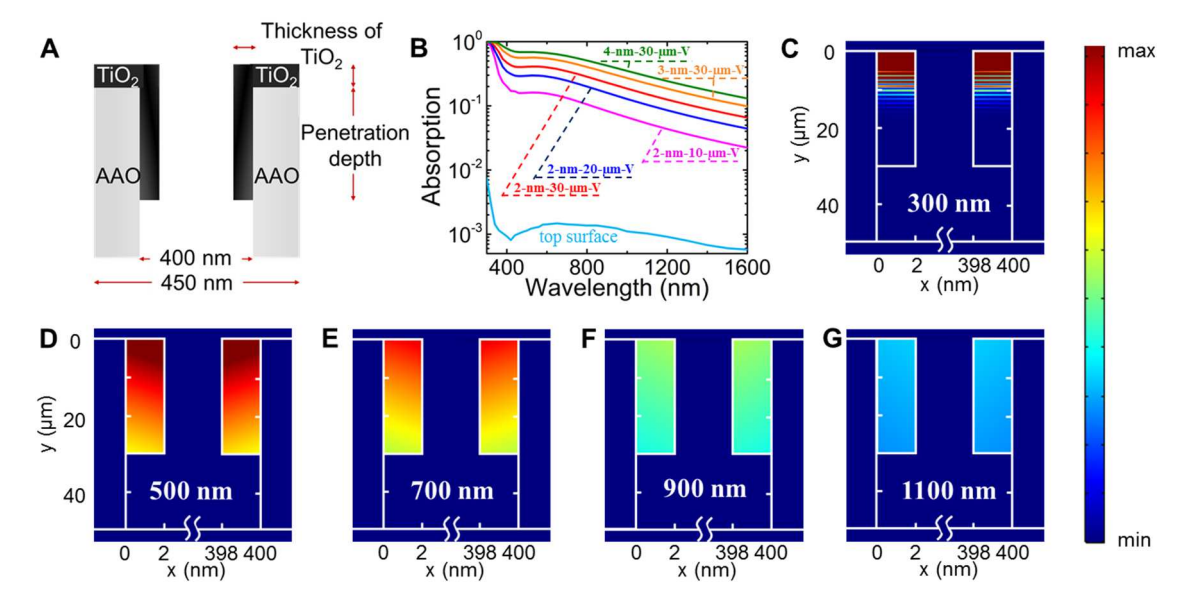


Fig. 3. (a) Schematic of the simulation model (not to scale for clarity). (b) Simulated optical absorption spectra in a 2-nm-thick TiO_x film at the top surface of AAO (cyan) and along the vertical direction of the nanopores with the penetration depth of 10 μm (magenta), 20 μm (blue), and 30 μm (red), respectively. The orange and green curves are simulated absorption spectra in the 3-nm- (orange) and 4-nm-thick (green) TiO_x film along the vertical direction of the nanopores, respectively, with the penetration depth of 30 μm. (c-g) Simulated absorption distribution along the vertical direction of the nanopores with the penetration depth of 30 μm at five different wavelengths: i.e., (c) 300 nm, (d) 500 nm, (e) 700 nm, (f) 900 nm, and (g) 1100 nm, respectively.

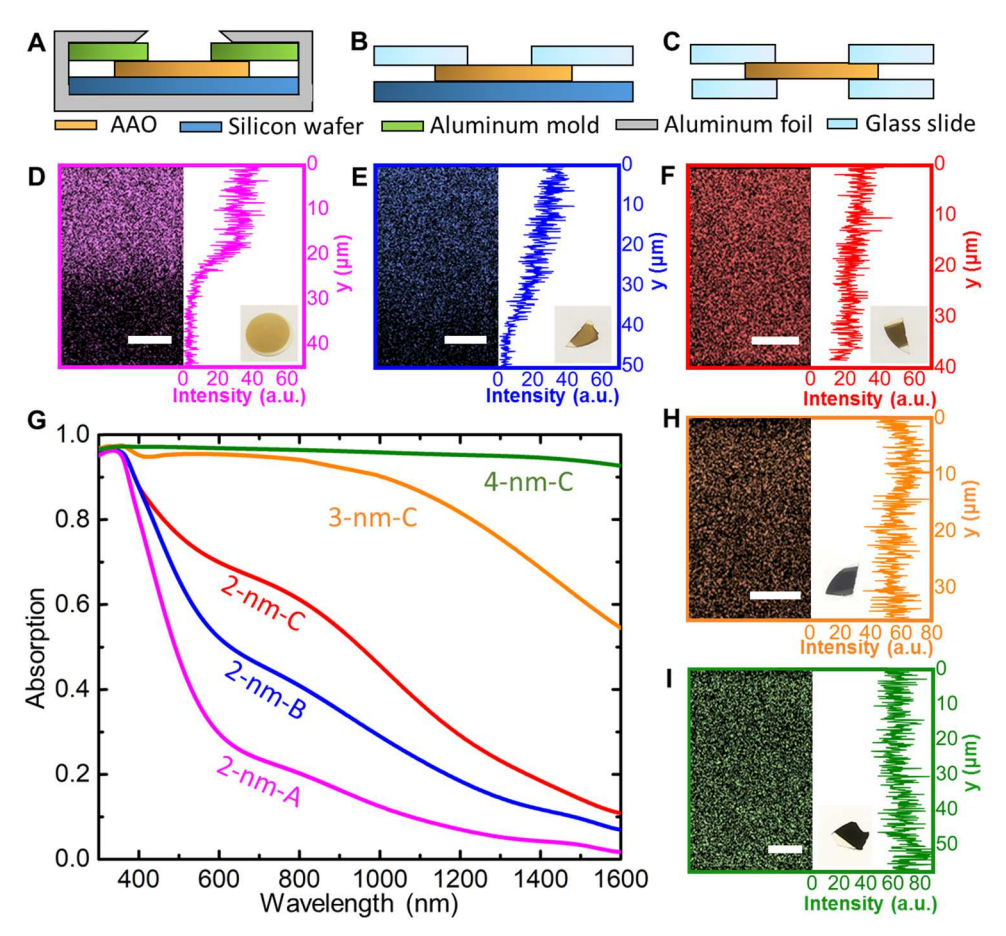


Fig. 4. (a-c) Schematics of (a) Setup A, (b) Setup B, and (c) Setup C, respectively. (d-f) Side-view EDS mapping of the Ti element (left panel) and line plots (right panel) of the 2-nm-thick TiO $_{\rm x}$ film in AAO fabricated using Setup A (d), Setup B (e), and Setup C (f), respectively. Scale bar: 10 µm. Insets: photographs of the samples. (g) Measured optical absorption spectra of five samples with the thickness from 2-nm to 4-nm fabricated by Setups A, B and C, respectively. (h-i) Side-view EDS mapping of Ti element (left panel) and line plots (right panel) of (h) 3-nm- and (i) 4-nm-thick TiO $_{\rm x}$ films in AAO made in Setup C. Scale bar: 10 µm. Insets: photographs of the samples.

(the 10-nm-thick- TiO_x /AAO samples shown in Figs. 1 and 2 were also deposited in this setup; see Section S6 in the Supporting Information). After the deposition of 2-nm-thick am- TiO_x thin film on the AAO templates (i.e., 52 ALD cycles with the deposition time of \sim 9 min), we

obtained three samples with obvious different optical absorption features as shown in the insets of Fig. 4D–F. In particular, Setup C resulted in the darkest sample. To reveal the distribution of $\mathrm{TiO}_{\mathrm{X}}$ thin film, EDS was employed to analyze the distribution of titanium element along the

pores. Both the element mapping images (left panels in Fig. 4D-F) and the corresponding line plots (right panels in Fig. 4D-F) indicated that the distribution of am-TiOx hollow nanotubes became more and more uniform from Setup A to Setup C. The measured absorption spectra (Fig. 4G) confirmed the absorption enhancement throughout the entire visible to IR region using Setup C (red curve) compared with Setups A (magenta curve) and B (blue curve). However, the absorption was still relatively low due to the ultra-small thickness. To achieve full spectrum solar light harvesting, we deposited 3-nm- and 4-nm-thick am-TiO_x films using Setup C and realized impressive optical absorption throughout the solar spectrum (i.e., orange and green curves in Fig. 4G, respectively) because of the more uniform distributed am-TiO_x films as shown by EDS results in Fig. 4H and 4I. In particular, the 4-nm-thick sample obtained an average absorption over 95%, with \sim 92% at the wavelength of 1.6 μ m. Importantly, this sample fabrication took ~18 min only for the film deposition (i.e., 104 cycles), much faster than previously reported synthesis methods to obtain dark TiOx nanoparticles (e.g. 4 h for magnesium reduction [9] or calcination [10]) or nanotubes (e.g. 1 h for high pressure hydrogen reduction [42], 4 h for melted aluminum reduction [44]). Although simple processes of cathodization in an aqueous electrolyte by reducing anodic TiO₂ nanotube arrays were also reported to realize dark TiO_v nanotubes (e.g [50,54–56].), the proposed ALD process is superior in thickness controllability down to Angstrom level (e.g [33].), which is crucial for the fabrication of ultra-thin or even atomically-thin TiOx films for more efficient optoelectronics and solar energy conversion applications. Besides, ALD process is more flexible and can enable the integration of ultra-thin TiOx nanostructures with different substrates that are needed in various applications. To demonstrate this wide tolerance in substrates, we employed commercial available glass fibers as the testbed and deposited 10-nm-thick am-TiO_x films on these porous substrates (see Section S7 in the Supporting Information). As shown in Fig. S6A, broadband optical absorption ranging from 65% to 90% can be realized on different glass fiber substrates, depending on their nominal pore sizes from 0.3 to 1.0 µm. This inexpensive, large scale and rapid manufacturing process is promising to integrate the am-TiO_x nanotubes with a wide selection of substrates and will enable the development of practical applications. Next, we will employ this type of dark am-TiOx nanotube array sample to demonstrate full spectrum solar energy harvesting and conversion applications.

3. Applications

Full spectrum solar absorption is highly desired in solar energy harvesting and conversion applications, for example, solar-driven photocatalysis [57–59] and solar vapor generation [60,61]. Thus we will demonstrate that the proposed dark ultra-thin am-TiO $_{\rm x}$ nanotube array could be leveraged to benefit these two representative applications.

3.1. Photocatalysis

We utilized the photoreduction of silver nitrate (AgNO₃) to Ag NPs as a testbed. This reaction is one of the methods to produce the Ag-TiO2 nanocomposite widely used in photocatalytic disinfections [62]. In previously reported works, photocatalytic performance of various dark TiO_x nanostructures and materials were evaluated by characterizing the size distribution of the product, Ag NPs (e.g [63,64].). As illustrated in Fig. 5A, in this experiment, we immersed the dark TiO_v/AAO into the AgNO₃ solution (0.5 mmol/L) for 90 s and illuminated it with a weak white light source through a UV filter with a cutoff wavelength of ~400 nm (see Fig. 5B for its optical spectrum, Section S8 in the Supporting Information for optical spectra of the other optical components; the power density is $\sim 9.6 \times 10^{-4} \text{ kW/m}^2$, ~ 3 orders of magnitude smaller than the regular solar intensity). Therefore, the photocatalytic effect was solely introduced by visible and infrared light (see Section S9 in the Supporting Information for photocatalytic experiments without the UV filter). The illumination time was changed from 0 s to 30 s, 60 s, and 90 s, and the corresponding products of Ag NPs were characterized by SEM in Fig. 5C-F, respectively (see enlarged SEM images in the insets for morphologies of Ag NPs). As shown in Fig. 5C, Ag NPs were generated without illumination due to the spontaneous reduction resulted from O [65]. Intriguingly, the size of the Ag NPs increased with longer illumination time (see white dots in Fig. 5D-F). For clarity, the size distributions were analyzed statistically in Fig. 5G (see details and the calculation data of the statistical analysis in Section S10 in the Supporting Information). As the illumination time increased from 0 s to 90 s (black for 0 s, red for 30 s, blue for 60 s, and magenta for 90 s in Fig. 5G), we obtained more Ag NPs in the range of 201-300 nm. In contrast, fewer NPs in the range of 101–150 nm were produced. To demonstrate the repeatability, another two sets of duplicated experiments were

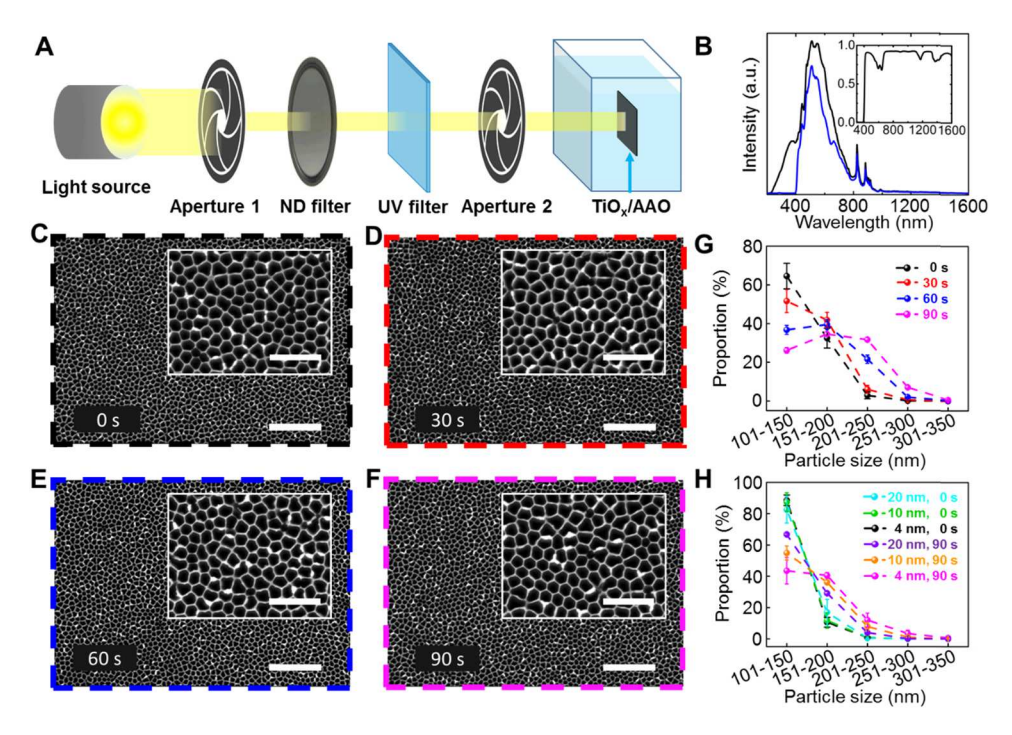


Fig. 5. (a) Schematic of the photocatalytic reduction of silver nitrate (AgNO3) using dark am-TiOx/AAO samples under visible and IR light illumination. (b) The intensity of light from the source (black) and transmitted through the UV filter (blue). Inset: The transmission spectrum of the UV filter. (c-f) Topview SEM images of the TiOx/AAO templates with the illumination time of (c) 0 s, (d) 30 s, (e) 60 s, and (f) 90 s, respectively. Scale bar: $5 \mu m$. Insets: Zoom-in views of different Ag NPs produced after the photocatalytic reduction. Scale bar: 2 µm. (g) Extracted statistic size distributions of Ag NPs with the illumination time of 0 s (black), 30 s (red), 60 s (blue), and 90 s (magenta), respectively, (h) Extracted statistic size distributions of Ag NPs on TiOx layers with different thicknesses and illumination time. Black curve: 4 nm and 0 s (i.e., dark). Magenta curve: 4 nm and 90 s. Green curve: 10 nm and 0 s. Orange curve: 10 nm and 90 s. Cyan curve: 20 nm and 0 s. Purple curve: 20 nm and 90 s. The total reaction time was 90 s for all samples.

presented in Section S11 in the Supporting Information, showing similar Ag NP production dependence on the illumination time. The distribution of Ag NPs along the vertical side walls of the nanopores is shown in Section S12 in the Supporting Information. On the other hand, no Ag NPs were found on annealed samples or bare AAO templates without am-TiO_x thin films under identical illumination conditions (see details in Section S13 and Section S14 in the Supporting Information).

Since this chemical reaction is heavily dependent on the reaction temperature, it is necessary to prove that our observation is from photocatalysis rather than from photothermal effects. Here we performed control experiments to reveal the thermal effect of the weak optical illumination on the dark am-TiOx/AAO sample. In the dark environment, the temperature of the AgNO₃ solution was increased by \sim 1 $^{\circ}$ C, which is much larger than the calculated temperature increase (i.e., 9.0×10^{-7} °C), assuming that all the light power is consumed by the AgNO₃ solution for temperature increase. No obvious change in Ag NP production was obtained (see more details in Section S15 in the Supporting Information). On the other hand, no Ag NPs were found on bare AAO templates without am-TiO_x thin films when the AgNO₃ solution was heated up by ~1 °C (see details in Section S14 in the Supporting Information). These control experiments demonstrated that the observed production of Ag NPs in Fig. 5 was introduced by photocatalytic effects rather than photothermal effects.

Importantly, the photocatalytic performance is highly dependent on the thickness of the dark TiOx layer. Although thicker TiOx films can realize similarly dark color (see Fig. S19A for optical absorption spectra of 10-nm- and 20-nm-thick TiO_x films in the Supporting Information), more recombination of photogenerated carriers occurred within those thicker films, restricting photocatalytic reactions. To validate this thickness-dependent photocatalytic performance, we conducted the photoreduction experiments using six more samples with the TiO_x thicknesses of 20 nm, 10 nm, and 4 nm, respectively (two samples for each thickness). The resulted Ag NPs are shown in SEM images in Section S16 in the Supporting Information. Since the optical absorption spectra of these samples were similar, the size distribution of these Ag NPs was mostly determined by the lifetime of the photogenerated carriers. As shown in Fig. 5H, the cyan, green, and black curves represented the size distributions of the Ag NPs on the 20-nm, 10-nm-, and 4-nmthick TiO_x films under the dark condition (i.e., the illumination time of 0 s), respectively. One can see that the three curves overlap with each other, indicating that the production of Ag NPs in dark was barely affected by the thickness of the TiO_x layer. After the illumination of 90 s, the size of the Ag NPs increased (see the purple curve for 20-nm sample, the orange curve for the 10-nm sample, and the magenta curve for the 4nm sample, respectively). One can see more large Ag NPs were produced on the 4-nm-thick TiO_x film (see the magenta curve). This experiment demonstrates the importance to achieve strong optical absorption in ultra-thin films and makes the dark am-TiO_x/AAO appealing to efficient full spectrum photocatalytic applications.

3.2. Photothermal effect

Next, we will further demonstrate the photothermal effect of am-TiO_x hollow nanotube array for full spectrum solar vapor generation. AAO-based nanostructures have been reported for efficient solar vapor generation in recent years. For instance, ~85-nm-thick Au [60] or Al films [61] were deposited on AAO templates to realize dark plasmonic architectures for efficient solar energy harvesting and thermal conversion. In our structure, we only deposited a 10-nm-thick am-TiO_x film on the AAO template and realized a broadband optical absorption throughout the solar spectrum (Fig. 1D). The hollow nanotube structure allows rapid transportation of water. On the other hand, the broadband solar absorption within the nanotubes is promising to realize efficient solar vapor generation. As shown by the thermal image in Fig. 6A, when the dark am-TiO_x hollow nanotube array sample was illuminated under 1 sun solar light (i.e., 1 kW/m²), its surface temperature was increased up to \sim 80 °C. In particular, this dark am-TiO $_x$ /AAO surface is very hydrophilic (see the hydrophilicity of the AAO templates in Section S17 in the Supporting Information). As shown in Fig. 6B, when the water droplet touched the sample surface, it immediately spread out and the contact angle was near zero (see details in the Experimental Section). Thus, the water filled into the nanopores can be evaporated rapidly due to the photothermal capability of this dark am-TiO_x/AAO sample. As shown in Fig. 6C and 6D, we placed the dark am-TiO_x/AAO on top of a \sim 4.9 cm² white paper (TexwipeTM TX609) on a foam floating at the water surface. Two strips of paper transported the underlying water to the upper surface of the paper. The AAO template on top of the paper continued the water transportation within the nanopores for evaporation (see details of the sample stability in Section S18 in the Supporting Information). Under 1 sun illumination (Fig. 6F), the surface temperature of the dark am-TiO $_x$ /AAO was ~39.0 °C (under the ambient temperature of 21.3 °C and humidity of 25%, respectively). The average evaporation rate was $\sim 1.29 \text{ kg/(m}^2 \text{ h})$ (Fig. 6E, see details in the Experimental Section), which is much higher than the natural evaporation rate of $\sim 0.12 \text{ kg/(m}^2 \text{ h})$ in dark environment. Therefore, the net increase in solar driven evaporation under 1 sun illumination is $\sim 1.17 \text{ kg/(m}^2 \text{ h})$. For comparison, we replaced the dark TiO_x/AAO sample with a bare AAO template without am-TiOx. Under the same 1 sun illumination, the average evaporation rate dropped to \sim 0.33 kg/(m² h) with a corresponding surface temperature of \sim 28.9 °C, demonstrating that the strong absorption of the dark TiOx/AAO efficiently facilitated the solar vapor generation.

Under moderate solar concentration conditions of 2, 3, 4, and 5 sun illumination, as shown in Fig. 6E, the vapor generation rates increased to $\sim\!2.50~kg/(m^2~h), \sim\!3.92~kg/(m^2~h), \sim\!4.86~kg/(m^2~h),$ and $\sim\!6.37~kg/(m^2~h)$, respectively. The corresponding surface temperature rose up to $\sim\!52.7~^\circ\text{C}, \sim\!61.0~^\circ\text{C}, \sim\!65.5~^\circ\text{C},$ and $\sim\!70.0~^\circ\text{C},$ respectively (Fig. 6G–J). By considering the incident energy and the energy consumption in evaporation, the solar thermal conversion efficiency of $\sim\!85.3\%$ and

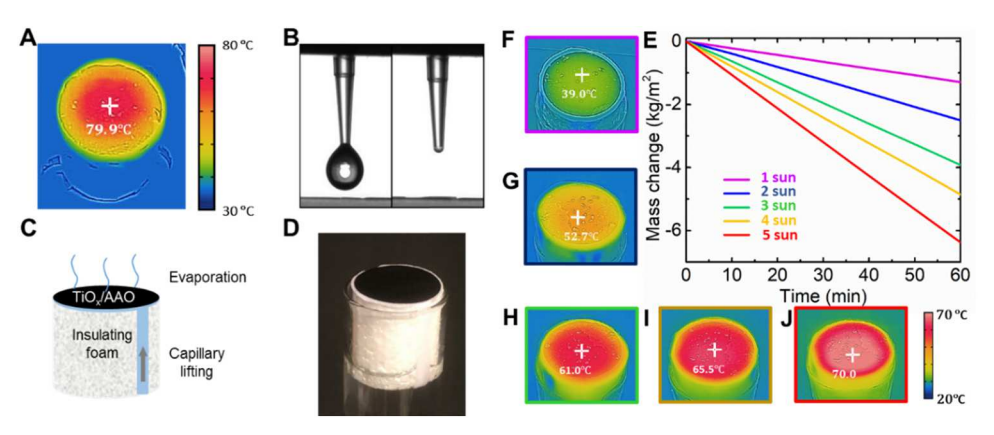


Fig. 6. (a) Thermal image of a dark am-TiO $_x$ / AAO sample under 1 sun illumination, characterized using a portable thermal imager (FLIR ONE Pro). (b) Water droplet on the dark am-TiO $_x$ /AAO sample. (c) The schematic and (d) the photograph of the thermal insulation architecture with a dark am-TiO $_x$ /AAO sample on top of a fabric paper and a floating foam. (e) The water mass change as a function of time under 1 (purple), 2 (blue), 3 (green), 4 (yellow), and 5 (red) sun illumination. (f-j) The corresponding thermal images of the dark TiO $_x$ /AAO sample under 1, 2, 3, 4, and 5 sun illumination.

 ${\sim}89.8\%$ were calculated under 1 and 5 sun illumination, respectively (see calculation details in Section S19 in the Supporting Information). Compared with previously reported AAO templates with Au [60] and Al NPs [61], this thermally safe and more cost-effective dark am-TiO_x/AAO architecture realized a very high solar thermal conversion efficiency, especially under 1 sun illumination (e.g. compared with ${\sim}64\%$ and ${\sim}58\%$ in [60,61] under 1 sun illumination, respectively). This is mainly due to the better thermal isolation introduced by the floating foam architecture [60,61,66] (see detailed comparison in Section 20 in the Supporting Information).

4. Experimental section

4.1. Fabrication of dark am-TiO_x/AAO

The AAO template was purchased from XFNANO Inc. The Ultratech/ Cambridge Nanotech Savannah S100 atomic layer deposition (ALD) system was used to deposit $\rm TiO_x$ on the AAO template. The precursors were tetrakis (dimethylamido)-titanium (TDMAT) and water. The COBRA BC 0100F pump with a normal pumping speed of 100 m $^3/h$ was employed in the ALD process. Initially, the reaction chamber was preheated to 250 °C when the precursor TDMAT was kept at 75 °C. Nitrogen was utilized as a precursor carrier gas at the flow rate of 20 standard cubic centimeters per minute. In the optimal ALD process, the feeding time for TDMAT and water were 0.1 s and 0.015 s, respectively. The purge time for both precursors were 5 s

4.2. Characterization

The morphology and chemical composition of the dark $\rm TiO_x/AAO$ was investigated by the scanning electron microscopy (SEM) and energy dispersive X-ray spectroscopy (EDS), respectively, using Carl Zeiss AURIGA FIB-SEM system. The transmission electron microscopy (TEM) images were obtained using an FEI Titan 80–300 TEM at an acceleration voltage of 300 kV. The light absorption was measured using the integration sphere spectroscopy (Thorlabs IS200-4 equipped with Ocean Optics USB 2000+ UV–VIS Spectrometer, Ocean Optics Jaz Portable Spectrometer, and AvaSpec-NIR256–1.7TEC for the UV-IR range), with a white high reflectance sphere material (manufactured from polytetrafluoroethylene based bulk material) as the reference. X-ray photoelectron spectroscopy (XPS) analysis was carried out by a Physical Electronics ESCA 5600 system using Al K α radiation to excite photoelectrons.

4.3. Electron paramagnetic resonance (EPR) spectroscopy

The dark TiO_x /AAO sample was grinded into small grain and put into a quartz EPR capillary tube with an inner diameter of 1.0 mm. The capillary tube was sealed by beeswax and then put into a larger quartz EPR sample tube with an outer diameter of 4.0 mm. It was then measured by Bruker EMX 390 EPR Spectrometer at room temperature.

4.4. Photocatalytic reduction of AgNO₃

As shown in Fig. 5, the light from the broadband light source (ENERGETIQ EQ-99XFC LDLS) was first collimated using a collimator (Thorlabs RC08SMA-F01), and then passed successively through Aperture 1 with a diameter of 1 mm, a neutral density filter (Thorlabs NDC-50C-4M), a UV filter (Chroma Autofluorescent Plastic Slides), and Aperture 2. The dark ${\rm TiO_x/AAO}$ sample was placed vertically in the center of the ${\rm AgNO_3}$ solution (0.5 mmol/L, 450 mL) stored in an acrylic container. The immersion time (i.e., reaction time) was 90 s for all samples and the illumination time was controlled by Aperture 2. After immersion, each sample was rinsed with deionized water for three times and then air dried vertically for 1 h. For better accuracy, each data point in the statistical analysis of the size distribution was based on three SEM

images at different locations.

4.5. Solar vapor generation measurements

The 100 mL graduated cylinder with the sample on top was illuminated by a solar simulator (Newport 69920 with AM 1.5 filter). The artificial sunlight intensity measured by a power meter (Thorlabs PM100D) with a thermal sensor (Thorlabs S305C, with a resolution of 0.1 mW) could be adjusted from one sun to five sun. A portable thermal imager (FLIR ONE Pro, with a resolution of 0.1 °C) was employed to characterize the temperature of the sample. The weight change of the evaporation system was measured by an electronic scale (Adam EBL 314i Eclipse® Analytical Balance, with a resolution of 0.1 mg) every ten minutes. The surface wetting property of the sample was measured using a CCD camera (FLIR USB2 camera, CMLN-13S2C-CS) capturing the 8 μL water droplet falling onto the sample surface.

5. Conclusions

In summary, we developed a facile one-step method using ALD process to fabricate ultra-thin am-TiO_x nanotubes on AAO templates. Due to the non-stoichiometric Ti³⁺ and O states as well as the structural features of the TiOx nanotube array on AAO substrates, the optical absorption band extends from UV (i.e., typical for traditional TiO2 materials) to visible and IR range. With an optimized 4-nm-thick am-TiO_x film, a strong absorption over 95% was obtained throughout the solar spectrum from 300 nm to 1.6 µm. Remarkably, the deposition time of this ultra-thin film is ~18 min only, much shorter than conventional strategies to realize dark ${\rm TiO_x}$ materials. In addition, the dark am- ${\rm TiO_x}/$ AAO samples exhibit great potential for photocatalysis and solar thermal applications. The reduction of AgNO3 solution to Ag NPs demonstrated the photocatalytic effect, which can be further explored for photocatalytic applications ranging from pollutant degradation [67], CO₂ reduction [68], to hydrogen production [69]. The photothermal capability of these dark hollow TiOx nanotubes was then demonstrated in solar vapor generation. With a simple thermal insulation architecture, a high solar thermal conversion efficiency of ~85.3% was achieved without any solar concentration. This type of dark semiconductor ultra-thin film materials may enable the development of simultaneous solar harvesting and energy conversion applications for sustainable energy and environmental investigation.

CRediT authorship contribution statement

Youhai Liu: Software, Validation, Formal analysis, Investigation, Data Curation, Writing - review & editing, Visualization. Haomin Song: Software, Formal analysis, Data Curation, Writing - original draft, Writing - review & editing, Visualization. Zongmin Bei: Investigation. Lyu Zhou: Investigation. Chao Zhao: Investigation. Boon S. Ooi: Resources, Investigation. Qiaoqiang Gan: Conceptualization, Methodology, Resources, Writing - review & editing, Visualization, Supervision, Funding acquisition.

Declaration of Competing Interest

The authors declare that they have no known competing financial interests or personal relationships that could have appeared to influence the work reported in this paper.

Acknowledgements

This study was partially supported by National Science Foundation (CBET-1932968). The authors appreciate Dr. Yu Han and Dr. Lingmei Liu's suggestion in TEM characterization at KAUST.

Appendix A. Supporting information

Supplementary data associated with this article can be found in the online version at doi:10.1016/j.nanoen.2021.105872.

References

- [1] T.S. Rajaraman, S.P. Parikh, V.G. Gandhi, Black TiO₂: a review of its properties and conflicting trends, Chem. Eng. J. 389 (2020), 123918.
- [2] X. Chen, L. Liu, F. Huang, Black titanium dioxide (TiO₂) nanomaterials, Chem. Soc. Rev. 44 (2015) 1861–1885.
- [3] A. Fujishima, K. Honda, Electrochemical photolysis of water at a semiconductor electrode, Nature 238 (1972) 37–38.
- [4] X. Liu, G. Zhu, X. Wang, X. Yuan, T. Lin, F. Huang, Progress in black titania: a new material for advanced photocatalysis, Adv. Energy Mater. 6 (2016), 1600452.
- [5] M. Xu, Y. Chen, J. Qin, Y. Feng, W. Li, W. Chen, J. Zhu, H. Li, Z. Bian, Unveiling the role of defects on oxygen activation and photodegradation of organic pollutants, Environ. Sci. Technol. 52 (2018) 13879–13886.
- [6] A. Naldoni, M. Altomare, G. Zoppellaro, N. Liu, S. Kment, R. Zboril, P. Schmuki, Photocatalysis with reduced TiO₂: from black TiO₂ to cocatalyst-free hydrogen production, ACS Catal. 9 (2019) 345–364.
- [7] Y. Zhao, Y. Zhao, R. Shi, B. Wang, G.I.N. Waterhouse, L.Z. Wu, C.H. Tung, T. Zhang, Tuning oxygen vacancies in ultrathin TiO₂ nanosheets to boost photocatalytic nitrogen fixation up to 700 nm, Adv. Mater. 31 (2019), 1806482.
- [8] X. Chen, L. Liu, Y.Y. Peter, S.S. Mao, Increasing solar absorption for photocatalysis with black hydrogenated titanium dioxide nanocrystals, Science 331 (2011) 746–750.
- [9] M. Ye, J. Jia, Z. Wu, C. Qian, R. Chen, P.G. O'Brien, W. Sun, Y. Dong, G.A. Ozin, Synthesis of black TiO_x nanoparticles by Mg reduction of TiO₂ nanocrystals and their application for solar water evaporation, Adv. Energy Mater. 7 (2017), 1601811.
- [10] X. Liu, B. Hou, G. Wang, Z. Cui, X. Zhu, X. Wang, Black titania/graphene oxide nanocomposite films with excellent photothermal property for solar steam generation, J. Mater. Res. 33 (2018) 674–684.
- [11] J. Wang, Y. Li, L. Deng, N. Wei, Y. Weng, S. Dong, D. Qi, J. Qiu, X. Chen, T. Wu, High-performance photothermal conversion of narrow-bandgap Ti₂O₃ nanoparticles, Adv. Mater. 29 (2017), 1603730.
- [12] F.H. Koppens, T. Mueller, P. Avouris, A.C. Ferrari, M.S. Vitiello, M. Polini, Photodetectors based on graphene, other two-dimensional materials and hybrid systems, Nat. Nanotechnol. 9 (2014) 780–793.
- [13] F. Xia, H. Wang, D. Xiao, M. Dubey, A. Ramasubramaniam, Two-dimensional material nanophotonics, Nat. Photon. 8 (2014) 899–907.
- [14] R.J. Shiue, X. Gan, Y. Gao, L. Li, X. Yao, A. Szep, D. Walker Jr, J. Hone, D. Englund, Enhanced photodetection in graphene-integrated photonic crystal cavity, Appl. Phys. Lett. 103 (2013), 241109.
- [15] X. Ge, M. Minkov, S. Fan, X. Li, W. Zhou, Laterally confined photonic crystal surface emitting laser incorporating monolayer tungsten disulfide, NPJ 2D Mater. Appl. 3 (2019) 16.
- [16] Y. Li, Z. Li, C. Chi, H. Shan, L. Zheng, Z. Fang, Plasmonics of 2D nanomaterials: properties and applications, Adv. Sci. 4 (2017), 1600430.
- [17] X. Li, J. Zhu, B. Wei, Hybrid nanostructures of metal/two-dimensional nanomaterials for plasmon-enhanced applications, Chem. Soc. Rev. 45 (2016) 3145–3187.
- [18] H. Song, L. Guo, Z. Liu, K. Liu, X. Zeng, D. Ji, N. Zhang, H. Hu, S. Jiang, Q. Gan, Nanocavity enhancement for ultra-thin film optical absorber, Adv. Mater. 26 (2014) 2737–2743.
- [19] Z. Xia, H. Song, M. Kim, M. Zhou, T.H. Chang, D. Liu, X. Yin, K. Xiong, H. Mi, X. Wang, F. Xia, Z. Yu, Z.J. Ma, Q. Gan, Single-crystalline germanium nanomembrane photodetectors on foreign nanocavities, Sci. Adv. 3 (2017), e1602783.
- [20] M.A. Kats, R. Blanchard, P. Genevet, F. Capasso, Nanometre optical coatings based on strong interference effects in highly absorbing media, Nat. Mater. 12 (2013) 20–24
- [21] H. Dotan, O. Kfir, E. Sharlin, O. Blank, M. Gross, I. Dumchin, G. Ankonina, A. Rothschild, Resonant light trapping in ultrathin films for water splitting, Nat. Mater. 12 (2013) 158–164.
- [22] C. Deng, H. Song, J. Parry, Y. Liu, S. He, X. Xu, Q. Gan, H. Zeng, Nanocavity induced light concentration for energy efficient heat assisted magnetic recording media, Nano Energy 50 (2018) 750–755.
- [23] H. Song, S. Jiang, D. Ji, X. Zeng, N. Zhang, K. Liu, C. Wang, Y. Xu, Q. Gan, Nanocavity absorption enhancement for two-dimensional material monolayer systems, Opt. Express 23 (2015) 7120–7130.
- [24] C. Janisch, H. Song, C. Zhou, Z. Lin, A.L. Elías, D. Ji, M. Terrones, Q. Gan, Z. Liu, MoS₂ monolayers on nanocavities: enhancement in light–matter interaction, 2D Mater. 3 (2016), 025017.
- [25] H. Song, W. Wu, J.W. Liang, P. Maity, Y. Shu, N.S. Wang, O.F. Mohammed, B. S. Ooi, Q. Gan, D. Liu, Ultrathin-film titania photocatalyst on nanocavity for CO₂ reduction with boosted catalytic efficiencies, Glob. Chall. 2 (2018), 1800032.
- [26] X. Chen, H.R. Park, M. Pelton, X. Piao, N.C. Lindquist, H. Im, Y.J. Kim, J.S. Ahn, K. J. Ahn, N. Park, D.S. Kim, S.H. Oh, Atomic layer lithography of wafer-scale nanogap arrays for extreme confinement of electromagnetic waves, Nat. Commun. 4 (2013) 2361.

[27] D. Yoo, F. de León-Pérez, M. Pelton, I.-H. Lee, D.A. Mohr, M.B. Raschke, J. D. Caldwell, L. Martín-Moreno, S.-H. Oh, Ultrastrong plasmon–phonon coupling via epsilon-near-zero nanocavities, Nat. Photon. 15 (2020) 125–130.

- [28] R.C. Devlin, M. Khorasaninejad, W.T. Chen, J. Oh, F. Capasso, Broadband high-efficiency dielectric metasurfaces for the visible spectrum, Proc. Natl. Acad. Sci. U. S. A. 113 (2016) 10473–10478.
- [29] S. Mubeen, J. Lee, N. Singh, S. Kramer, G.D. Stucky, M. Moskovits, An autonomous photosynthetic device in which all charge carriers derive from surface plasmons, Nat. Nanotechnol. 8 (2013) 247–251.
- [30] M.S. Sander, M.J. Côté, W. Gu, B.M. Kile, C.P. Tripp, Template-assisted fabrication of dense, aligned arrays of titania nanotubes with well-controlled dimensions on substrates, Adv. Mater. 16 (2004) 2052–2057.
- [31] R.J. Narayan, N.A. Monteiro-Riviere, R.L. Brigmon, M.J. Pellin, J.W. Elam, Atomic layer deposition of TiO₂ thin films on nanoporous alumina templates: medical applications, JOM 61 (2009) 12–16.
- [32] Q. Xie, Y.L. Jiang, C. Detavernier, D. Deduytsche, R.L. Van Meirhaeghe, G.P. Ru, B. Z. Li, X.P. Qu, Atomic layer deposition of TiO₂ from tetrakis-dimethyl-amido titanium or Ti isopropoxide precursors and H₂O, J. Appl. Phys. 102 (2007), 083521.
- [33] R.W. Johnson, A. Hultqvist, S.F. Bent, A brief review of atomic layer deposition: from fundamentals to applications, Mater. Today 17 (2014) 236–246.
- [34] D. Zhao, B. Xu, J. Yang, J. Wu, W. Zhai, B. Yang, M. Liu, Interfacial diffusion of hydrated ion on graphene surface: a molecular simulation study, Langmuir 36 (2020) 13613–13620.
- [35] X. Chen, C. Meng, Y. Wang, Q. Zhao, Y.J. Li, X.M. Chen, D. Yang, Y. Li, Y. Zhou, Laser-synthesized rutile TiO₂ with abundant oxygen vacancies for enhanced solar water evaporation, ACS Sustain. Chem. Eng. 8 (2020) 1095–1101.
- [36] Z. Pei, L. Ding, H. Lin, S. Weng, Z. Zheng, Y. Hou, P. Liu, Facile synthesis of defect-mediated TiO_{2-x} with enhanced visible light photocatalytic activity, J. Mater. Chem. A 1 (2013) 10099.
- [37] J.W. Yun, K.Y. Ryu, T.K. Nguyen, F. Ullah, Y.C. Park, Y.S. Kim, Tuning optical band gap by electrochemical reduction in TiO₂ nanorods for improving photocatalytic activities, RSC Adv. 7 (2017) 6202–6208.
- [38] G. Li, Z. Lian, X. Li, Y. Xu, W. Wang, D. Zhang, F. Tian, H. Li, Ionothermal synthesis of black Ti^{3+} -doped single-crystal TiO_2 as an active photocatalyst for pollutant degradation and H_2 generation, J. Mater. Chem. A 3 (2015) 3748–3756.
- [39] V.A. Zuniga-Ibarra, S. Shaji, B. Krishnan, J. Johny, S.S. Kanakkillam, D. A. Avellaneda, J.A. Aguilar Martinez, T.K. Das Roy, N.A. Ramos-Delgado, Synthesis and characterization of black TiO₂ nanoparticles by pulsed laser irradiation in liquid, Appl. Surf. Sci. 483 (2019) 156–164.
- [40] S.G. Ullattil, P. Periyat, Green microwave switching from oxygen rich yellow anatase to oxygen vacancy rich black anatase TiO₂ solar photocatalyst using Mn(ii) as 'anatase phase purifier', Nanoscale 7 (2015) 19184–19192.
 [41] C. Fan, C. Chen, J. Wang, X. Fu, Z. Ren, G. Qian, Z. Wang, Black hydroxylated
- [41] C. Fan, C. Chen, J. Wang, X. Fu, Z. Ren, G. Qian, Z. Wang, Black hydroxylated titanium dioxide prepared via ultrasonication with enhanced photocatalytic activity, Sci. Rep. 5 (2015) 11712.
- [42] N. Liu, C. Schneider, D. Freitag, M. Hartmann, U. Venkatesan, J. Muller, E. Spiecker, P. Schmuki, Black TiO₂ nanotubes: cocatalyst-free open-circuit hydrogen generation, Nano Lett. 14 (2014) 3309–3313.
- [43] N. Liu, V. Haublein, X. Zhou, U. Venkatesan, M. Hartmann, M. Mackovic, T. Nakajima, E. Spiecker, A. Osvet, L. Frey, P. Schmuki, "Black" TiO₂ nanotubes formed by high-energy proton implantation show noble-metal-co-catalyst free photocatalytic H₂-evolution, Nano Lett. 15 (2015) 6815–6820.
- [44] H. Cui, W. Zhao, C. Yang, H. Yin, T. Lin, Y. Shan, Y. Xie, H. Gu, F. Huang, Black TiO₂ nanotube arrays for high-efficiency photoelectrochemical water-splitting, J. Mater. Chem. A 2 (2014) 8612–8616.
- [45] M. Liang, X. Li, L. Jiang, P. Ran, H. Wang, X. Chen, C. Xu, M. Tian, S. Wang, J. Zhang, T. Cui, L. Qu, Femtosecond laser mediated fabrication of micro/nanostructured TiO_{2-x} photoelectrodes: hierarchical nanotubes array with oxygen vacancies and their photocatalysis properties, Appl. Catal. B-Environ. 277 (2020), 119231.
- [46] T. Siefke, S. Kroker, K. Pfeiffer, O. Puffky, K. Dietrich, D. Franta, I. Ohlídal, A. Szeghalmi, E.B. Kley, A. Tünnermann, Materials pushing the application limits of wire grid polarizers further into the deep ultraviolet spectral range, Adv. Opt. Mater. 4 (2016) 1780–1786.
- [47] M. Gaintantzopoulou, S. Zinelis, N. Silikas, G. Eliades, Micro-Raman spectroscopic analysis of TiO₂ phases on the root surfaces of commercial dental implants, Dent. Mater. 30 (2014) 861–867.
- [48] J. Xu, Z. Tian, G. Yin, T. Lin, F. Huang, Controllable reduced black titania with enhanced photoelectrochemical water splitting performance, Dalton Trans. 46 (2017) 1047–1051.
- [49] S.A. Abdullah, M.Z. Sahdan, N. Nafarizal, H. Saim, Z. Embong, C.H.C. Rohaida, F. Adriyanto, Influence of substrate annealing on inducing Ti³⁺ and oxygen vacancy in TiO₂ thin films deposited via RF magnetron sputtering, Appl. Surf. Sci. 462 (2018) 575–582.
- [50] Z. Li, H. Bian, X. Xiao, J. Shen, C. Zhao, J. Lu, Y.Y. Li, Defective black TiO₂ nanotube arrays for enhanced photocatalytic and photoelectrochemical applications, ACS Appl. Nano Mater. 2 (2019) 7372–7378.
- [51] Y. Li, W. Wang, F. Wang, L. Di, S. Yang, S. Zhu, Y. Yao, C. Ma, B. Dai, F. Yu, Nanomaterials (2019) 9.
- [52] Y. Ju, M. Wang, Y. Wang, S. Wang, C. Fu, Adv. Condens. Matter Phys. (2013) 2013.
- [53] R. Boidin, T. Halenkovič, V. Nazabal, L. Beneš, P. Němec, Pulsed laser deposited alumina thin films, Ceram. Int. 42 (2016) 1177–1182.
- [54] H. Zhou, Y. Zhang, Electrochemically self-doped TiO₂ nanotube arrays for supercapacitors, J. Phys. Chem. C 118 (2014) 5626–5636.

- [55] Y. Yang, M.R. Hoffmann, Synthesis and stabilization of blue-black TiO₂ nanotube arrays for electrochemical oxidant generation and wastewater treatment, Environ. Sci. Technol. 50 (2016) 11888–11894.
- [56] N. Liu, C. Schneider, D. Freitag, E.M. Zolnhofer, K. Meyer, P. Schmuki, Noble-metal-free photocatalytic H₂ generation: active and inactive 'Black' TiO₂ nanotubes and synergistic effects, Chem. A Eur. J. 22 (2016) 13810–13814.
- [57] X. Gan, D. Lei, R. Ye, H. Zhao, K.Y. Wong, Nano Res. (2020) 1-20.
- [58] X. Gan, D. Lei, K.Y. Wong, Two-dimensional layered nanomaterials for visible-light-driven photocatalytic water splitting, Mater. Today Energy 10 (2018) 352–367.
- [59] M. Shen, Z. Yan, L. Yang, P. Du, J. Zhang, B. Xiang, MoS₂ nanosheet/TiO₂ nanowire hybrid nanostructures for enhanced visible-light photocatalytic activities, Chem. Commun. 50 (2014) 15447–15449.
- [60] L. Zhou, Y. Tan, D. Ji, B. Zhu, P. Zhang, J. Xu, Q. Gan, Z. Yu, J. Zhu, Self-assembly of highly efficient, broadband plasmonic absorbers for solar steam generation, Sci. Adv. 2 (2016), e1501227.
- [61] L. Zhou, Y. Tan, J. Wang, W. Xu, Y. Yuan, W. Cai, S. Zhu, J. Zhu, 3D self-assembly of aluminium nanoparticles for plasmon-enhanced solar desalination, Nat. Photon. 10 (2016) 393–398.
- [62] T. An, H. Zhao, P.K. Wong, Advances in Photocatalytic Disinfection, Springer, 2017

- [63] Y. Wu, W. Yang, Y. Fan, Q. Song, S. Xiao, TiO₂ metasurfaces: from visible planar photonics to photochemistry, Sci. Adv. 5 (2019), eaax0939.
- [64] L. Huttenhofer, F. Eckmann, A. Lauri, J. Cambiasso, E. Pensa, Y. Li, E. Cortes, I. D. Sharp, S.A. Maier, Anapole excitations in oxygen-vacancy-rich TiO_{2-x} nanoresonators: tuning the absorption for photocatalysis in the visible spectrum, ACS Nano 14 (2020) 2456–2464.
- [65] X. Pan, Y.J. Xu, Fast and spontaneous reduction of gold ions over oxygen-vacancyrich TiO₂: a novel strategy to design defect-based composite photocatalyst, Appl. Catal. A Gen. 459 (2013) 34–40.
- [66] H. Ghasemi, G. Ni, A.M. Marconnet, J. Loomis, S. Yerci, N. Miljkovic, G. Chen, Solar steam generation by heat localization, Nat. Commun. 5 (2014) 4449.
- [67] J. Lim, Y. Yang, M.R. Hoffmann, Activation of peroxymonosulfate by oxygen vacancies-enriched cobalt-doped black TiO₂ nanotubes for the removal of organic pollutants, Environ. Sci. Technol. 53 (2019) 6972–6980.
- [68] T. Billo, F.Y. Fu, P. Raghunath, I. Shown, W.F. Chen, H.T. Lien, T.H. Shen, J.F. Lee, T.S. Chan, K.Y. Huang, C.I. Wu, M.C. Lin, J.S. Hwang, C.H. Lee, L.C. Chen, K. H. Chen, Ni-nanocluster modified black TiO₂ with dual active sites for selective photocatalytic CO₂ reduction, Small 14 (2018), 1702928.
- [69] W. Zhou, W. Li, J.Q. Wang, Y. Qu, Y. Yang, Y. Xie, K. Zhang, L. Wang, H. Fu, D. Zhao, Ordered mesoporous black TiO₂ as highly efficient hydrogen evolution photocatalyst, J. Am. Chem. Soc. 136 (2014) 9280–9283.